Article

Direct-bonded diamond membranes for heterogeneous quantum and electronic technologies

Xinghan Guo[1], Mouzhe Xie [1,2,6], Anchita Addhya[1,6], Avery Linder [1,6], Uri Zvi [1], Stella Wang [3], Xiaofei Yu[3], Tanvi D. Deshmukh[3], Yuzi Liu [4], Ian N. Hammock[1], Zixi Li [1], Clayton T. DeVault [1,5], Amy Butcher[1], Aaron P. Esser-Kahn [1], David D. Awschalom [1,3,5], Nazar Delegan[1,5], Peter C. Maurer [1,5], F. Joseph Heremans [1,5] & Alexander A. High [1,5] ✉

Diamond has superlative material properties for a broad range of quantum and electronic technologies. However, heteroepitaxial growth of single crystal diamond remains limited, impeding integration and evolution of diamond-based technologies. Here, we directly bond single-crystal diamond membranes to a wide variety of materials including silicon, fused silica, sapphire, thermal oxide, and lithium niobate. Our bonding process combines customized membrane synthesis, transfer, and dry surface functionalization, allowing for minimal contamination while providing pathways for near unity yield and scalability. We generate bonded crystalline membranes with thickness as low as 10 nm, sub-nm interfacial regions, and nanometer-scale thickness variability over 200 by 200 μm^2 areas. We measure spin coherence times T_2 for nitrogen vacancy centers in 150 nm-thick bonded membranes of up to $623 \pm 21\,\mu$s, suitable for advanced quantum applications. We demonstrate multiple methods for integrating high quality factor nanophotonic cavities with the diamond heterostructures, highlighting the platform versatility in quantum photonic applications. Furthermore, we show that our ultra-thin diamond membranes are compatible with total internal reflection fluorescence (TIRF) microscopy, which enables interfacing coherent diamond quantum sensors with living cells while rejecting unwanted background luminescence. The processes demonstrated herein provide a full toolkit to synthesize heterogeneous diamond-based hybrid systems for quantum and electronic technologies.

Diamond is broadly proposed for future quantum and electronic technologies. For example, color centers in diamond offer exceptional coherence properties[1,2] and robust spin-photon interfaces[3,4]. This enabled recent progress on quantum networking demonstrations[5,6]

and quantum sensing applications, notably nuclear magnetic resonance (NMR) spectroscopy[7], magnetometry[8], and electrometry[9]. Further evolution of these technologies requires heterogeneous material platforms to expand on-chip functionalities, including nonlinear

[1]Pritzker School of Molecular Engineering, University of Chicago, Chicago, IL 60637, USA. [2]School of Molecular Sciences, Arizona State University, Tempe, AZ 85287, USA. [3]Department of Physics, University of Chicago, Chicago, IL 60637, USA. [4]Center for Nanoscale Materials, Argonne National Laboratory, Lemont, IL 60439, USA. [5]Center for Molecular Engineering and Materials Science Division, Argonne National Laboratory, Lemont, IL 60439, USA. [6]These authors contributed equally: Mouzhe Xie, Anchita Addhya, Avery Linder. ✉e-mail: ahigh@uchicago.edu

photonics, microfluidics, acoustics, electronics, detectors, and light sources. Moreover, diamond has best-in-class figures-of-merit for several applications in power electronics and these technologies can similarly benefit from heterogeneous integration[10–12]. However, single-crystal diamond-based heterostructures are challenging to be synthesized directly due to the technical difficulty of heteroepitaxial overgrowth[13]. Alternatively, multiple approaches have been demonstrated to integrate thin film diamond, utilizing Van der Waals forces[14,15] or intermediary bonding layers such as epoxy[16] and hydrogen silsesquioxane (HSQ)[17]. While promising, a truly generic approach—robust to fabrication and integration processes without introducing defects, decoherence sources, or superfluous materials—is still missing. In reference, multi-material heterostructures are commonly generated via wafer bonding, a manufacturing process that is foundational to modern electronic technologies. By chemically bonding films of disparate materials, wafer bonding allows high-quality crystalline materials to be combined in instances where direct growth processes are insufficient.

In this work, we introduce surface plasma activation based synthesis of diamond heterostructures where diamond membranes are directly bonded to technologically relevant materials, including silicon, fused silica, thermal oxide, sapphire, and lithium niobate ($LiNbO_3$), with the capability of pre-existing on-chip structures. The bonded membranes obtain atomically smooth surfaces, precise thickness, pristine material quality, and uniform interfaces while maintaining the spin coherence of color centers. Furthermore, we show that fabricated nanophotonic cavities exhibit low optical losses, and membranes containing nitrogen-vacancy (NV-) centers are straightforwardly integrated with microfluidic flow channels for quantum bio-sensing and imaging, highlighting the potential of this material platform for quantum and electronic applications.

Results
Membrane bonding

The flow diagram of the full bonding process is shown in Fig. 1. The fabrication process begins with membrane synthesis via smart-cut[18], followed by homoepitaxial diamond overgrowth and ex situ or in situ color center formation. Substrates are then patterned to define individual membrane shapes via either photo- or electron-beam lithography. Target membranes are undercut by selectively removing sp^2 carbon via electrochemical (EC) etching, leaving a small tether attached to the diamond substrate for deterministic manipulation. Membrane overgrowth, patterning, and EC etching are detailed in our previous work[19]. Here, we limit our membrane sizes to 200 μm by 200 μm squares. Larger and more intricate membrane shapes can be generated by extending the EC etching time and slightly modifying the patterning step of the process flow.

Following EC etching, we utilize templated area-controlled poly-dimethylsiloxane (PDMS) stamps to transfer and manipulate membranes with improved process yield and scalability[20]. This transfer process is shown in Fig. 1a. The PDMS stamps have two different patterns, allowing for smaller (PDMS1-stamp) and larger (PDMS2-stamp) contact areas, and by extension, adhesion strength (see Supplementary Section 1.2). PDMS1-stamp is used to break the diamond tether and pick up the membrane, whereas PDMS2-stamp is used for flipping the diamond membrane from PDMS1-stamp and subsequent placement. In both cases, the prominence of the adhesion region, which is 50 μm taller than the rest of the stamp, ensures only the targeted membrane is contacted. This method enables multiple membrane transfers following EC etching, which, in the future, can be automated into a single step for the entire diamond substrate.

Next, we remove the underlying diamond layer that was damaged by He+ implantation. This improves the overall crystallographic quality and fully decouples the final membranes, which are isotopically pur-
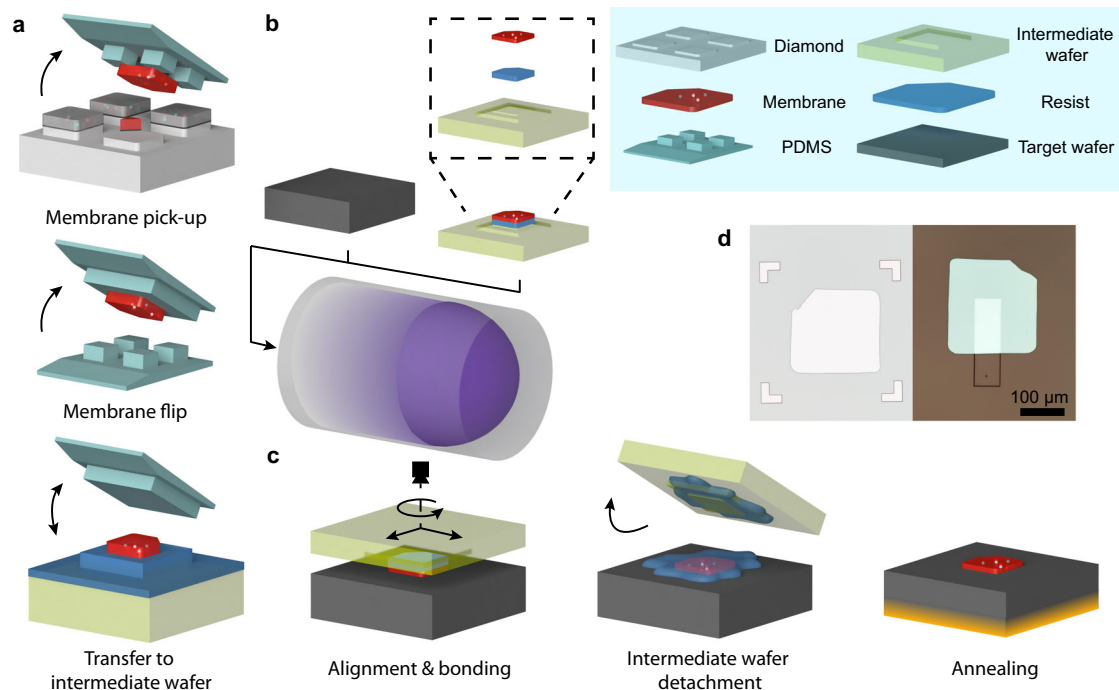
Fig. 1 | Schematics of the plasma-activated bonding of diamond membranes. a Diamond membrane transfer to the intermediate wafer. From top to down: membrane pick-up from the diamond substrate using PDMS1-stamp, membrane flipping with PDMS2-stamp, membrane placement to a photoresist or electron beam resist covered intermediate wafer. **b** Diamond back etching and downstream oxygen plasma treatment. Inset: the detailed layer stack of the ICP-etched intermediate wafer. **c** Plasma-activated membrane bonding. Left to right: membrane alignment and bonding, temperature-controlled intermediate wafer detachment, and post-bonding annealing. **d** Microscope images of 155-nm-thick diamond membranes bonded to a thermal oxide substrate with markers (left) and a fused silica substrate with a 5-μm-deep trench etched prior to bonding (right).

ified with controlled doping, from the low-cost type-IIa diamond substrate. This thinning is performed via inductively coupled plasma (ICP) reactive ion etching (RIE). To protect the final bonded substrate from being etched, we thin the membrane by placing it on an intermediate fused silica carrier wafer. Intermediate wafers are coated with photo- (AZ1505) or electron beam resist (PMMA), which softens in the temperature range from 100 to 130 °C with reduced viscosity at subsequent stages. This additional step flips the membrane again so the growth side is facing up (exposed) on the target substrate, which eliminates growth side morphology constraints for bonding and enables precise depth control for near-surface and δ-doped color centers. To prevent the resist from overheating and crosslinking, we developed a multi-cycle etching recipe with short plasma duration of ≤15 s per cycle. The schematic of the etched intermediate wafer is shown as the inset of Fig. 1b; additional information can be found in Supplementary Section 1.4. Using this methodology, we realize precise thickness control from 10 nm to 500 nm. The maximum thickness is determined by the homoepitaxial overgrowth step and can be modified to meet application needs.

We utilize a downstream O_2 plasma ashing for surface activation on both the diamond membrane and target substrate to enable subsequent bonding (Fig. 1b). The target substrates are subjected to a high power ashing recipe (gas flow 200 sccm, RF power 600 W for 150 s) with extended process duration for inert substrates such as sapphire and $LiNbO_3$. The membranes receive either this high power recipe or an O_2 descum clean (gas flow 100 sccm, RF power 200 W for 25 s), which does not etch nor roughen the diamond surface. The downstream O_2 plasma cleans and oxygen-terminates (see Supplementary Section 3.4) the membrane and carrier material surfaces without the need for wet processing[21,22]. To prevent functionalization degradation at elevated temperatures (see Supplementary Section 2.4), all ashing recipes are performed at room temperature.

Next, we bond the membrane to the target substrate, as shown in Fig. 1c. We mount the patterned intermediate wafer onto a micropositioner-controlled glass slide via a flat, chip-size PDMS stamp. The target substrate is vacuum secured on a temperature-controlled stage. Leveraging optical access through the transparent intermediate wafer for alignment, we move the membrane to the target location and bring it into contact with the target substrate, which coincides with the appearance of membrane-scale interference fringes/patterns (see Supplementary Section 1.6). Using this method, we achieve an alignment precision of 30 μm and 0.1°. We sequentially heat the heterostructure by elevating the temperature of the stage through multiple steps (also see Supplementary Section 1.6). After reaching the resist softening point, we slide the intermediate wafer away, leaving the bonded structure behind. Future utilization of dedicated wafer-bonding equipment will significantly improve the precision and tolerance of all transfer steps.

Finally, to ensure a robust, covalently bonded interface between the membrane and the target wafer, we anneal the heterostructure at 550° under argon forming gas atmosphere to minimize undesired oxidation. This annealing also removes the polymethyl methacrylate (PMMA) residue and leaves a clean direct-bonded membrane as the final product if PMMA-based transfer is applied (see Supplementary Section 1.7 for in-depth discussions)[23]. A micrograph of a membrane-thermal oxide heterostructure with pre-defined markers is shown on the left of Fig. 1d, revealing a high alignment accuracy. The right of Fig. 1d shows a membrane bonded to a fused silica trench, emphasizing our capability of bonding membranes to structured materials. The overall process yield stands above 95%, limited by inconsistent plasma ashing chamber conditions and the poorly controlled approach angle of the transfer station, which can be readily improved by transitioning to process specific tooling.

Material characterization

In-depth material characterization reveals the preserved diamond quality throughout the bonding process. We utilize atomic force microscopy (AFM) to characterize the membrane surface morphology, which is a critical determinant not only for successful plasma-activated bonding, but also the coherence and stability of near-surface color centers[24]. As shown in Fig. 2a, both small and large area scanning results returned atomically flat surface profiles with $R_q \leq 0.3$ nm. Additionally, we characterize target substrates via AFM to ensure sub-nm roughness post plasma treatments as detailed in Supplementary Table S1.

Beyond local height variation, the bonded membrane shows a general flatness of ≈ 1 nm, as characterized via profilometry. The thickness profile of the membrane, shown in Fig. 2b, reveals a uniform height of 493.7 ± 1.1 nm, with the standard deviation less than the instrument resolution (1.5 nm) for large scale scanning. Beyond line scans, a two dimensional flatness map of the membrane is studied via confocal laser scanning microscopy, and is detailed in Supplementary Section 2.3.

The effectiveness of the plasma surface activation is characterized by tracking the change in surface hydrophilicity of the bonding interfaces via contact angle measurements[25,26], as shown in Fig. 2c. For the diamond surface, the contact angle reduces from 52.4° ± 0.7° to 6.1° post high power plasma treatment, indicating a considerable increase in hydrophilicity. This is confirmed via quantitative X-ray photoelectron spectroscopy (XPS) characterization of surface species also shown in Fig. 2c (see Supplementary Section 2.6 for more details). We note that surface hydrophilicity is directly correlated with a reduction of surface amorphous carbon sp^2 bonds as quantified by the more reliable D-parameter extrapolation of the C KLL line[27,28]. Furthermore, the decrease from the raw C 1s quantification (likely an increase of ether-like terminations[24]) and an increase of surface available sapphire-O bonds indicate an effective surface preparation and oxygen termination to both surfaces. Similar behavior is confirmed on all target bonding materials with observed contact angles below 20° post treatments.

The quality of the bonded diamond heterostructure is directly studied via high resolution transmission electron microscopy (HRTEM). Figure 2d, e show a uniformly ICP-thinned (from ≈ 309 nm to 10 ± 0.3 nm while the lateral dimension remains to be 200 μm × 200 μm) diamond membrane bonded to a sapphire substrate. The thinness and uniformity reflect the high level of process control and allows single field of view characterization of both diamond membrane interfaces. The HRTEM image reveals several critical features. Firstly, the membrane exhibits uniform crystallinity and morphology throughout its thickness. Secondly, we observe a sharp, sub-0.5 nm interface between the crystalline diamond and sapphire. Thirdly, there is a repeating atomic arrangement throughout the interface profile, evidence of a covalently cross-linked interface[29–32]. Energy Dispersive X-ray Spectroscopy (EDS) analysis of the various elements associated with the intersection (C, Al, O) places an upper limit on the bonding interface to be less than 2 nm (see Supplementary Section 2.5). We note that the EDS analysis artificially broadens the interface as a result of the slight angular mismatch between the electron beam depth projection and the actual physical interface.

Furthermore, we characterize the optical properties of group IV color centers in the bonded membranes. Confocal imaging reveals that germanium vacancies (GeV⁻) within the bonded membranes have high signal-to-background and sufficient optical coherence for applications in quantum technologies. Figure 2c shows a typical photoluminescence (PL) map of individual GeV⁻ centers hosted in a membrane bonded to a distributed Bragg reflector (DBR) mirror at 4K. The signal-to-background ratio of GeV⁻ can be as large as ≈ 65 with an average value of ≈ 40, a significant improvement from any suspended HSQ-based membranes (5–30) and bulk diamond (≈ 25)[19]. The bonding
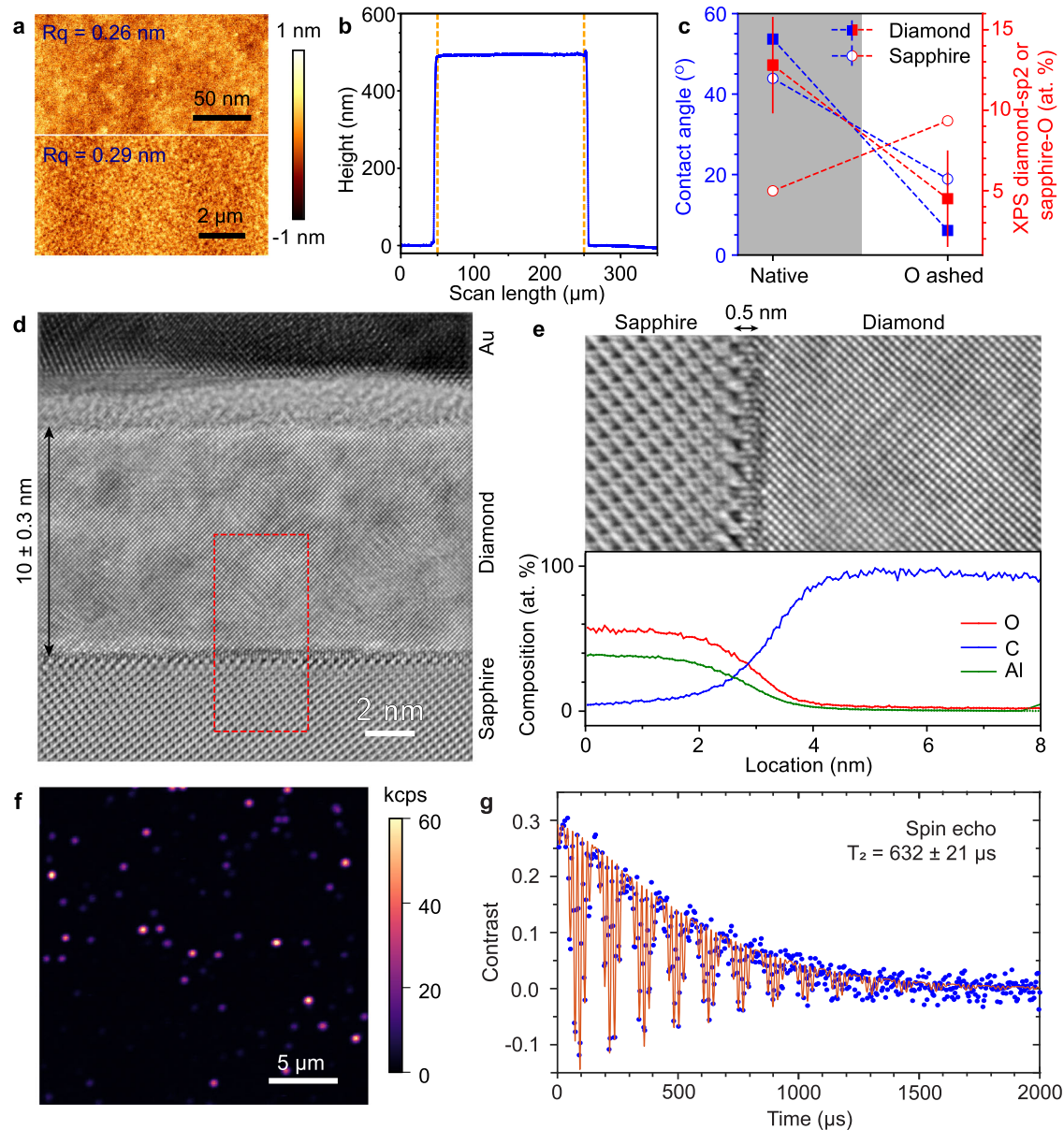
Fig. 2 | Characterization of the bonded membrane. a AFM of the diamond bonding interface (the etched side) post ICP etching. Atomically flat surfaces with $R_q \leq 0.3$ nm were observed in both small (200 nm by 100 nm, the upper figure) and large (10 μm by 5 μm, the lower figure) scanning areas. **b** Profilometry of a membrane-silicon heterostructure. The membrane region is highlighted by two dashed orange lines. The thickness of the membrane is 493.7 nm with a standard deviation of 1.1 nm. **c** The contact angle and XPS of diamond and sapphire pre- and post- high power plasma treatments. An increase of hydrophilicity is observed via the decrease of the contact angle, and the effect of oxygen termination is observed through the reduction of the carbon sp² as obtained from C KLL extrapolation of the sp²/sp³ ratio and the enhancement of the sapphire-O signals as obtained from the O 1s peak quantification. **d** HRTEM image of a 10-nm-thick membrane bonded to a c-plane sapphire substrate. The 2 nm intermediate layer on top of diamond comes from the lack of surface control before gold deposition. **e** Top: the zoomed-in HRTEM image of the diamond-sapphire bonding interface, the red dashed rectangle region in **d**, showing a sub-0.5 nm thickness of the bonding intersection. Bottom: EDS elemental analysis across the bonding interface. **f** The PL map of GeV centers in a membrane bonded to a DBR mirror at 4 K. The signal-to-background ratio around the zero phonon line (ZPL) can be as high as 65, with the signal surpassing 65 kc s⁻¹. **g** Hahn-echo measurements of one typical NV⁻ at room temperature showing a T_2 value of 632 ± 21 μs. See Supplementary Section 5.7 for data acquisition and fitting details.

process also preserves GeV⁻ centers' optical coherence and introduces minimal strain, as shown in the Supplementary Sections 3.2 and 3.3.

Lastly, to examine the compatibility of qubits in direct-bonded membranes with quantum technologies, we investigate the spin properties of NV⁻ centers in an $\approx$ 150-nm-thick diamond membrane bonded to a thermal oxide substrate. Room temperature measurements of a NV⁻ center show a remarkably long Hahn-echo T_2 of 632 ± 21 μs (Fig. 2g) and a Ramsey T_2 of 92 ± 16 μs (See Supplementary Section 5.7). These coherence times are comparable to the 600 μs to 2000 μs coherence times reported in isotopically purified

bulk diamond[33] and are suitable for high-performance quantum sensing[34–36]. The spin echo oscillation originates from the nuclear spin of a nearby ¹³C atom (see Supplementary Section 5.7 for details).

Quantum technologies with bonded diamond membranes
Here we demonstrate the suitability of diamond-based heterogeneous material platforms for quantum technologies. First, we explore nanophotonic integration, which improves qubit addressability and is broadly utilized in quantum photonics. Photonic integration is commonly achieved by patterning diamond into undercut, suspended
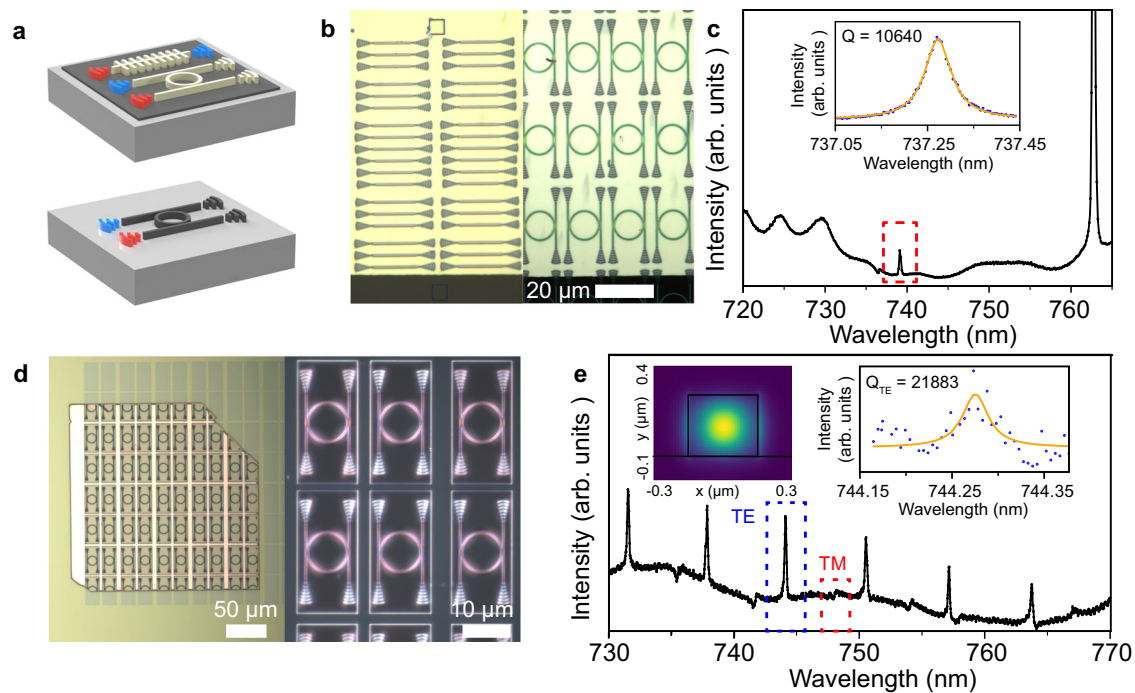
Fig. 3 | Nanophotonic integration with direct-bonded membranes. a Schematics of TiO_2-based (top) and diamond-based (bottom) nanophotonics on diamond membrane heterostructures. In this work fused silica (thermal oxide silicon) wafers are used as carrier wafers for the TiO_2 (diamond)-based demonstrations. The grating couplers for excitation (collection) are colored in red (blue), respectively. **b** Microscope images of TiO_2 fishbone cavities and ring resonators on a 50 nm-thick diamond membrane. Images were taken at the same location but different fabrication rounds. **c** The transmission spectrum of a fishbone cavity with resonant frequency at 737.26 nm. Inset: the transmission of the cavity with a tunable laser as the excitation source, showing a quality factor Q of 10640 ± 118. **d** The bright field and dark field microscope images of the ICP-etched diamond ring resonators on a thermal oxide silicon substrate, showing great uniformity with minimal process contamination. **e** The transmission spectrum of the diamond-based ring resonator measured at the drop port. Insets: the TE mode profile, and the TE cavity resonance with a quality factor Q_{TE} of 21883 ± 6284. The fluctuation in the right inset is caused by the instability of the optical setup.

structures, creating geometrical constraints that complicate further multiplexing and integration with on-chip single-photon detectors, electronics, or other devices that could enhance quantum network functionality. Here, we show that our bonded membranes enable multiple approaches to photonic integration.

First, we utilize templated atomic layer deposition (ALD) of TiO_2 to create nanophotonic devices on the surface of a 50 nm-thick membrane bonded to a fused silica substrate (see Supplementary Section 4.2.1 for fabrication details)[37]. The schematic is shown as the upper image of Fig. 3a, with excitation and collection ports (grating couplers) colored in red and blue, respectively. In these devices, the optical mode effectively hybridizes between the TiO_2 and diamond. Separate microscope images of TiO_2 fishbone cavities and ring resonators are shown in Fig. 3b. These images were taken at the same location but different fabrication rounds, highlighting the robustness of the membranes to cleanroom processing and the recyclability of photonic integration.

Transmission measurements of the cavities reveal significant improvement of quality factors. The transmission spectrum of a typical fishbone cavity with target wavelength 737 nm − the wavelength of SiV emission − is shown in Fig. 3c. The highest measured quality factor Q is 10640, with a three device average of 10150 ± 350. These values are 2.5 times higher than our previous demonstration[37], resulting from elimination of the bonding layer and the improvement of the diamond crystal quality. We also predict a maximum Purcell enhancement factor of 270 in the diamond based on updated Q factors. These metrics are suitable for state-of-the-art experiments in cavity quantum electrodynamics[38]. Similarly, ring resonators measured through the drop port exhibit quality factors as $Q_{TM} = 16319$ ($Q_{TE} = 12620$) for transverse magnetic, TM (transverse electric, TE) modes (see Supplementary Section 4.2.2 for details).

Next, to explore the robustness of our bonded diamond platform to direct photonics integration, we etch nanophotonic ring resonators directly into a 280 nm-thick diamond membrane using a lithographically defined hard mask and a single RIE step. This is simplified in comparison to the angular etching or isotropic etching methods commonly used to create suspended diamond photonics from monolithic bulk diamond[15,39]. The schematic is shown in the lower image of Fig. 3a. Bright and dark field images of the devices are shown in Fig. 3d, demonstrating the high quality and uniformity of the fabrication process. As plotted in Fig. 3e, one of these ring resonators exhibits quality factors Q of 21883 ± 6284 at visible wavelength range, with large field confinement within the diamond. Although this value looks slightly lower than the best-reported visible-wavelength quality factors 3×10^4 to 6×10^4 for diamond[40], our finesse $F = 188.4$ is higher than the value calculated from the previous work (≈ 69.4) due to the use of a much smaller ring diameter, and thus, a wider free spectral range (FSR). We note that in telecommunications wavelengths, previous demonstrations of diamond ring resonators have shown quality factors $Q \sim 1.14 \times 10^6$ [41]. Combined with a separate demonstration of high quality photonic crystal cavities with Q up to 1.8×10^5 in our direct-bonded membranes that are subsequently suspended[42], our platform supports a broad range of photonic integration. Additionally, our platform enables direct integration with other visible-frequency photonic platforms including lithium niobate, silicon nitride, and titanium dioxide, as well as on-chip light sources and detectors, and thus paves a path for hybrid quantum photonic technologies.

Diamond heterostructures also have distinct advantages in quantum metrology, such as nanoscale magnetic field[43,44], electric field[45], and temperature sensing[46,47]. In these applications a diamond sensor is typically brought in close proximity of a sensing target. The most sensitive diamond sensors rely on high-purity single-crystals with
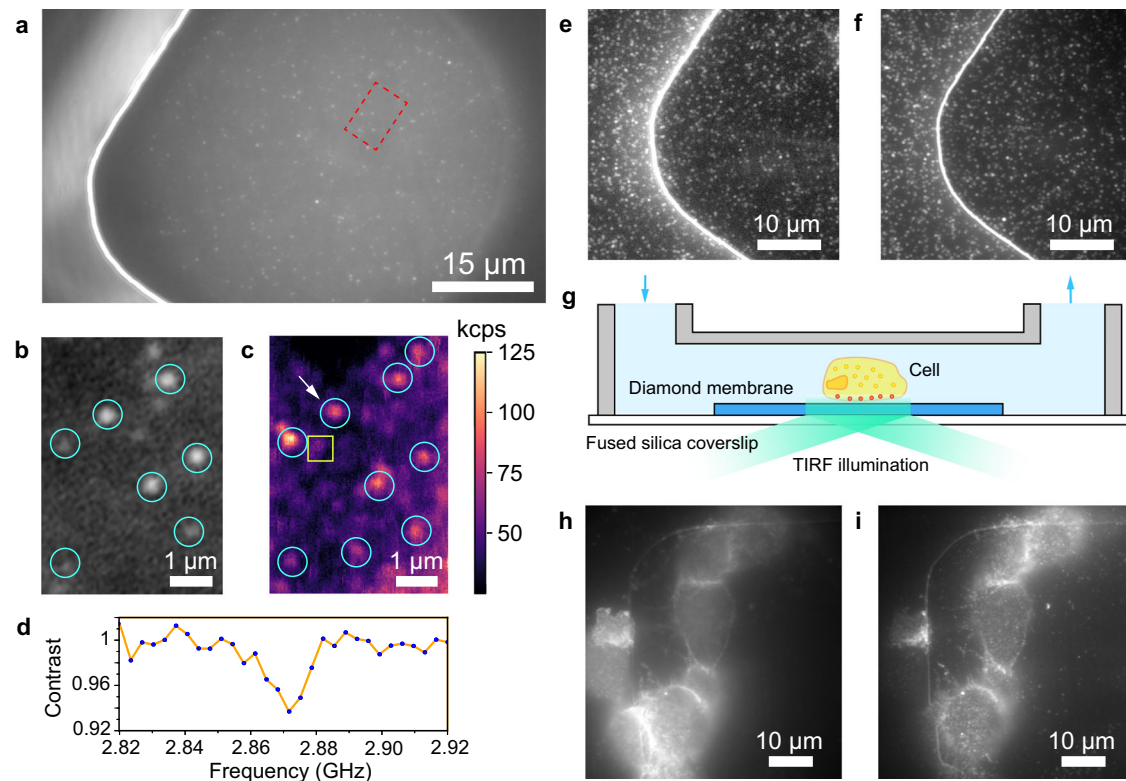
Fig. 4 | Imaging of NV⁻ centers and surface-attached target molecules and cells in a flow channel. a Widefield fluorescence microscopy image of a diamond membrane corner containing NV⁻ centers at room temperature. Only a round area in the center was illuminated to avoid back-reflection from membrane edges. **b** The zoomed-in image of the boxed region shown in **a** post rotation. **c** A confocal scan of the same region as **b** using a separate setup at room temperature. Emitters confirmed to be (not) NV⁻ centers are highlighted in cyan circles (yellow boxes). Same symbols are used in **b**. **d** A representative CW-ODMR spectrum from the NV⁻ center labeled with a white arrow in **c**. Additional studies of NV⁻ spin coherence are included in the Supplementary Section 5.7. **e, f** Widefield fluorescence microscopy images of (**e**) Alexa-488-labeled streptavidin protein and (**f**) streptavidin-conjugated Qdot-525 quantum dots that were immobilized at the same region shown in **a** via biotinylated surface functionalization. **g** Schematic illustration of the flow channel structure and a cell illuminated by total internal reflection through the diamond membrane. Fluorescence microscopy images of Alexa-488-labeled TLR2 receptors on RAW cell surfaces, under (**h**) episcopic and (**i**) objective-based TIRF illumination. Edges of the diamond membrane are also visible in these images.

the sensing target bound on the diamond's top surface[48]. The large thickness and refractive index of conventional bulk diamond requires optical initialization and readout of the sensing qubits from the top surface. As a consequence of this geometry, the target systems need to possess optical transparency, low auto-fluorescence, and high photo-stability, which are significant restrictions for the study of biological systems. Bonded membranes overcome these challenges by enabling optical addressability through the back of the membrane, without the need for passing through the top surface and the sensing target.

First, we investigate the stability and addressability of individual NV⁻ centers (i.e., our qubit sensor) in bonded diamond membranes. Figure 4 (a)-(c) shows individually resolvable photostable NV⁻ centers in a 160 nm-thick membrane bonded to a fused silica coverslip in widefield and confocal imaging. These emitters are confirmed to be NV⁻ centers through the presence of their characteristic 2.87 GHz zero-field splitting by optically detected magnetic resonance (ODMR) spectroscopy (Fig. 4d). NV⁻ centers in membranes were previously reported (and in this work) to have excellent spin coherence[19]. Next, we chemically functionalized the heterostructure surface using a technique recently developed for bulk diamond[49]. Using back illumination of our diamond membranes, we show that the fluorescence of individual Alexa488-labeled streptavidin molecules (Fig. 4e) and streptavidin-conjugated Qdot-525 quantum dots (Fig. 4f) can be detected. This enables localization of not only NV-centers but also the fluorescent sensing targets bound to the membrane's surface (also see Supplementary Section 5.3.4 for

simultaneous detection). The ability to fluorescently detect the position of individual NV⁻ centers and proteins is important for NV-based single-molecule nuclear magnetic resonance[50] and electron paramagnetic resonance[51] spectroscopy, as this will allow for the efficient identification of NV⁻ centers that have a desired molecular target within the sensing range.

We also combine our bonded diamond membranes with TIRF-microscopy to demonstrate imaging at a reduced level of background luminescence. Figure 4g shows a schematic representation of a diamond membrane integrated in a flow channel with macrophage-like RAW cells grown on the diamond surface. Optical excitation above the critical angle ensures that only a small section above the diamond membrane is excited by the optical field. Staining the toll-like receptor 2 (TLR2) with Alexa488-labeled anti-TLR2 antibody reveals in TIRF imaging the location of individual protein distributed across cell surface (Fig. 4i). This is in stark contrast with the epiluminescence mode where background luminescence prevents the imaging of individual molecules (Fig. 4h). We note that the larger index of refraction ($n = 2.4$) of diamond results in an evanescent field that falls 1.6-times faster off compared with a conventional glass microscope coverslip ($n = 1.5$) (see Supplementary Section 5.6). Likewise, we show the sedimentation of living *Escherichia coli* bacteria on the diamond membrane introduced via a flow channel (see Supplementary Video 1). Experiments enabled by the flow channel demonstrate remarkable flexibility to interface target samples with quantum diamond sensors, which is challenging to be fulfilled through conventional approaches[52].

Discussions

We have demonstrated a complete process flow to create diamond-based heterogenous materials and technologies. The bonded membranes combine isotopic engineering, in situ doping, and precise thickness control, while maintaining the surface morphology, flatness, and crystal quality necessary for quantum technologies. We generated bonded, continuous crystalline films as thin as 10 nm, well below previous demonstrations and comparable to material geometries in state-of-the-art microelectronics[17,19,53]. HRTEM reveals ordered, sub-nanometer bond interfaces, PL measurements demonstrate high signal-to-background ratio for all hosted color centers, and nitrogen vacancy centers maintain bulk-like spin coherence. The process is compatible with nano-structured substrates, has a compact footprint and requires no post-bond etching, ensuring the integrity of pre-existing target substrate structures. Bonded membranes are robust to multiple subsequent nanofabrication steps, and our method is compatible with standard semiconductor manufacturing processes including wafer-bonding.

Crucially, by avoiding intermediary adhesion materials, we generate optimal material heterostructures for applications in quantum photonics and quantum biosensing. Technological suitability for quantum photonics is demonstrated via the integration of high quality factor nanophotonics by either TiO_2 deposition or direct diamond patterning and etching. These diamond-based heterostructures, with minimal optical loss, are ideal candidates for on-chip nanophotonic integration and spin-photon coupling devices. Furthermore, we demonstrate that diamond membrane bonding unlocks novel experimental possibilities for quantum biosensing and imaging by integrating flow channels with diamond membranes. The simultaneous resolution of fluorescent molecules and NV^- centers will enable accurate identification of proximal NV^- sensors for desired sensing targets. The ultrathin diamond membranes also allow for TIRF illumination which strongly improves the signal contrast of local sensing targets while minimizing undesired laser excitation.

Our manufacturing process opens up a broad range of heterogeneous diamond-based platforms for quantum technologies. The integration of diamond with electro-optical and piezoelectric materials such as $LiNbO_3$ will pave the ways for on-chip, electrically-reconfigurable nonlinear quantum photonics and allow studies of quantum spin-phonon interactions[54,55]. Diamond bonding unlocks additional coupling possibilities with other solid state qubits, magnonic hybrid systems, or superconducting platforms[35,56–58]. Furthermore, combining our diamond membranes with established techniques for the creation of highly coherent near-surface NV^- centers[19,24] will result in ultra-sensitive diamond-probes optimized for the study of molecular binding assays[59], two dimensional dichalcogenides (TMD)[60], and thin-film magnetic materials[61]. Lastly, with high thermal conductivity, large bandgap and high critical electric field, bonded diamond membranes have myriad applications in high power electronics[10–12].

Data availability

The data related to the fabrication process, materials characterization, and optical measurements are provided with this paper or displayed in the Supplementary Information. All other data is available from the corresponding author upon request. Source data are provided with this paper.

References

1. Abobeih, M. H. et al. One-second coherence for a single electron spin coupled to a multi-qubit nuclear-spin environment. *Nat. Commun.* **9**, 1 (2018).
2. Sukachev, D. D. et al. Silicon-Vacancy Spin Qubit in Diamond: A Quantum Memory Exceeding 10 ms with Single-Shot State Read-out. *Phys. Rev. Lett.* **119**, 1 (2017).
3. Bernien, H. et al. Heralded entanglement between solid-state qubits separated by three metres. *Nature* **497**, 86 (2013).
4. Debroux, R. et al. Quantum Control of the Tin-Vacancy Spin Qubit in Diamond. *Phys. Rev. X* **11**, 41041 (2021).
5. Abobeih, M. H. et al. Atomic-scale imaging of a 27-nuclear-spin cluster using a quantum sensor. *Nature* **576**, 411 (2019).
6. Bhaskar, M. K. et al. Experimental demonstration of memory-enhanced quantum communication. *Nature* **580**, 60 (2020).
7. Devience, S. J. et al. Nanoscale NMR spectroscopy and imaging of multiple nuclear species. *Nat. Nanotechnol.* **10**, 129 (2015).
8. Jenkins, A. et al. Imaging the Breakdown of Ohmic Transport in Graphene. *Phys. Rev. Lett.* **129**, 87701 (2022).
9. Yang, B. et al. Vector Electrometry in a Wide-Gap-Semiconductor Device Using a Spin-Ensemble Quantum Sensor. *Phys. Rev. Appl.* **14**, 1 (2020).
10. Donato, N., Rouger, N., Pernot, J., Longobardi, G. & Udrea, F. Diamond power devices: state of the art, modelling, figures of merit and future perspective. *J. Phys. D Appl. Phys.* **53**, 093001 (2019).
11. Chow, T. P., Omura, I., Higashiwaki, M., Kawarada, H. & Pala, V. Smart power devices and ics using gaas and wide and extreme bandgap semiconductors. *IEEE Trans. Electron Devices* **64**, 856 (2017).
12. Perez, G. et al. Diamond semiconductor performances in power electronics applications. *Diam. Relat. Mater.* **110**, 108154 (2020).
13. Gallheber, B.-C., Fischer, M., Mayr, M., Straub, J. & Schreck, M. Growth, stress, and defects of heteroepitaxial diamond on Ir/YSZ/Si(111). *J. Appl. Phys.* **123**, 225302 (2018).
14. Høy Jensen, R. et al. Cavity-Enhanced Photon Emission from a Single Germanium-Vacancy Center in a Diamond Membrane. *Phys. Rev. Appl.* **13**, 64016 (2020).
15. Wan, N. H. et al. Large-scale integration of artificial atoms in hybrid photonic circuits. *Nature* **583**, 226 (2020).
16. Smits, J. et al. Two-dimensional nuclear magnetic resonance spectroscopy with a microfluidic diamond quantum sensor. *Sci. Adv.* **5**, 1 (2019).
17. Jung, T. et al. Reproducible fabrication and characterization of diamond membranes for photonic crystal cavities. *Phys. Status Solidi a* **213**, 3254 (2016).
18. Aharonovich, I. et al. Homoepitaxial Growth of Single Crystal Diamond Membranes for Quantum Information Processing. *Adv. Mater.* **24**, OP54 (2012).
19. Guo, X. et al. Tunable and transferable diamond membranes for integrated quantum technologies. *Nano Lett.* **21**, 10392 (2021).
20. Dibos, A. M., Raha, M., Phenicie, C. M. & Thompson, J. D. Atomic source of single photons in the telecom band. *Phys. Rev. Lett.* **120**, 243601 (2018).
21. Matsumae, T. et al. Low-temperature direct bonding of β-Ga_2O_3 and diamond substrates under atmospheric conditions. *Appl. Phys. Lett.* **116**, 141602 (2020).
22. Liang, J., Masuya, S., Kasu, M. & Shigekawa, N. Realization of direct bonding of single crystal diamond and si substrates. *Appl. Phys. Lett.* **110**, 111603 (2017).
23. Zhuang, B., Li, S., Li, S. & Yin, J. Ways to eliminate pmma residues on graphene – superclean graphene. *Carbon* **173**, 609 (2021).
24. Sangtawesin, S. et al. Origins of Diamond Surface Noise Probed by Correlating Single-Spin Measurements with Surface Spectroscopy. *Phys. Rev. X* **9**, 31052 (2019).
25. Salvadori, M. et al. Termination of diamond surfaces with hydrogen, oxygen and fluorine using a small, simple plasma gun. *Diam. Relat. Mater.* **19**, 324 (2010).
26. Yamamoto, M. et al. Comparison of argon and oxygen plasma treatments for ambient room-temperature wafer-scale au-au bonding using ultrathin au films. *Micromachines* **10**, 2 (2019).
27. Mezzi, A. & Kaciulis, S. Surface investigation of carbon films: from diamond to graphite. *Surf. Interface Anal.* **42**, 1082 (2010).

28. Lesiak, B. et al. C sp2/sp3 hybridisations in carbon nanomaterials - XPS and (X)AES study. *Appl. Surf. Sci.* **452**, 223 (2018).
29. Talneau, A. et al. Atomic-plane-thick reconstruction across the interface during heteroepitaxial bonding of InP-clad quantum wells on silicon. *Appl. Phys. Lett.* **102**, 212101 (2013).
30. Chandrasekaran, N., Soga, T. & Jimbo, T. GaAs film on Si substrate transplanted from GaAs/Ge structure by direct bonding. *Appl. Phys. Lett.* **82**, 3892 (2003).
31. Gösele, U. & Tong, Q.-Y. Semiconductor wafer bonding. *Annu. Rev. Mater. Sci.* **28**, 215 (1998).
32. Razek, N. et al. Low temperature covalent wafer bonding for x-ray imaging detectors. *Jpn. J. Appl. Phys.* **59**, SBBB06 (2019).
33. Balasubramanian, G. et al. Ultralong spin coherence time in isotopically engineered diamond. *Nat. Mater.* **8**, 383 (2009).
34. Barry, J. F. et al. Sensitivity optimization for NV-diamond magnetometry. *Rev. Mod. Phys.* **92**, 15004 (2020).
35. Fukami, M., Candido, D. R., Awschalom, D. D. & Flatté, M. E. Opportunities for long-range magnon-mediated entanglement of spin qubits via on- and off-resonant coupling. *PRX Quantum* **2**, 040314 (2021).
36. Candido, D. R., Fuchs, G. D., Johnston-Halperin, E. & Flatté, M. E. Predicted strong coupling of solid-state spins via a single magnon mode. *Mater. Quantum Technol.* **1**, 011001 (2020).
37. Butcher, A. et al. High-Q Nanophotonic Resonators on Diamond Membranes using Templated Atomic Layer Deposition of TiO2. *Nano Lett.* **20**, 4603 (2020).
38. Nguyen, C. T. et al. An integrated nanophotonic quantum register based on silicon-vacancy spins in diamond. *Phys. Rev. B* **100**, 165428 (2019).
39. Burek, M. J. et al. Free-standing mechanical and photonic nanostructures in single-crystal diamond. *Nano Lett.* **12**, 6084–6089 (2012).
40. Burek, M. J. et al. High quality-factor optical nanocavities in bulk single-crystal diamond, *Nat. Commun.* **5**, 5718 (2014).
41. Hausmann, B. J., Bulu, I., Venkataraman, V., Deotare, P. & Loncar, M. Diamond nonlinear photonics. *Nat. Photonics* **8**, 369 (2014).
42. Ding, S. W. et al. High-q cavity interface for color centers in thin film diamond. *Nat. Commun.* **15**, 6358 (2024).
43. Balasubramanian, G. et al. Nanoscale imaging magnetometry with diamond spins under ambient conditions. *Nature* **455**, 648 (2008).
44. Maze, J. R. et al. Nanoscale magnetic sensing with an individual electronic spin in diamond. *Nature* **455**, 644 (2008).
45. Dolde, F. et al. Electric-field sensing using single diamond spins. *Nat. Phys.* **7**, 459 (2011).
46. Kucsko, G. et al. Nanometre-scale thermometry in a living cell. *Nature* **500**, 54 (2013).
47. Toyli, D. M. et al. Fluorescence thermometry enhanced by the quantum coherence of single spins in diamond. *Proc. Natl Acad. Sci. USA* **110**, 8417 (2013).
48. Schirhagl, R., Chang, K., Loretz, M. & Degen, C. L. Nitrogen-vacancy centers in diamond: Nanoscale sensors for physics and biology. *Annu. Rev. Phys. Chem.* **65**, 83–105 (2014).
49. Xie, M. et al. Biocompatible surface functionalization architecture for a diamond quantum sensor. *Proc. Natl Acad. Sci. USA* **119**, e2114186119 (2022).
50. Lovchinsky, I. et al. Nuclear magnetic resonance detection and spectroscopy of single proteins using quantum logic. *Science* **351**, 836 (2016).
51. Shi, F. et al. Single-protein spin resonance spectroscopy under ambient conditions. *Science* **347**, 1135 (2015).
52. Glenn, D. R. et al. High-resolution magnetic resonance spectroscopy using a solid-state spin sensor. *Nature* **555**, 351 (2018).
53. Ruf, M. et al. Optically Coherent Nitrogen-Vacancy Centers in Micrometer-Thin Etched Diamond Membranes. *Nano Lett.* **19**, 3987 (2019).
54. Maity, S. et al. Coherent acoustic control of a single silicon vacancy spin in diamond. *Nat. Commun.* **11**, 193 (2020).
55. Maity, S. et al. Mechanical control of a single nuclear spin. *Phys. Rev. X* **12**, 011056 (2022).
56. Marcos, D. et al. Coupling nitrogen-vacancy centers in diamond to superconducting flux qubits. *Phys. Rev. Lett.* **105**, 210501 (2010).
57. Kubo, Y. et al. Hybrid quantum circuit with a superconducting qubit coupled to a spin ensemble. *Phys. Rev. Lett.* **107**, 220501 (2011).
58. Awschalom, D. D. et al. Quantum Engineering With Hybrid Magnonics Systems and Materials. *IEEE Trans. Quantum Eng.* **2**, 1 (2021).
59. Shi, F. et al. Single-DNA electron spin resonance spectroscopy in aqueous solutions. *Nat. Methods* **15**, 697 (2018).
60. Zhou, B. B. et al. Spatiotemporal mapping of a photocurrent vortex in monolayer MoS$_2$ using diamond quantum sensors. *Phys. Rev. X* **10**, 011003 (2020).
61. Sun, Q. C. et al. Magnetic domains and domain wall pinning in atomically thin CrBr$_3$ revealed by nanoscale imaging. *Nat. Commun.* **12**, 1989 (2021).

Acknowledgements

Author contributions

X.G. and A.A.H. conceived the experiment; X.G. and A.L. developed the bonding technique and fabricated the membrane samples; T.D.D., I.N.H., and C.T.D. contributed to the bonding technique development; X.G., Y.L., and N.D. performed the material analysis; A.A. and A.B. designed and fabricated the photonic devices; M.X. and U.Z. fabricated the sensing devices, X.G., M.X., A.A., U.Z., X.Y., S.W., and Z.L. performed optical measurements and data analysis; X.G. wrote the manuscript with input from all co-authors; A.A.H., F.J.H., P.C.M., N.D., D.D.A., and A.P.E.-K. participated in and supervised the project.

Competing interests

X.G., A.A.H., T.D.D., A.L., I.N.H., N.D., C.T.D., and F.J.H. filed a PCT (International) patent for the methods of bonding diamond membranes.

Additional information

Supplementary information The online version contains supplementary material available at https://doi.org/10.1038/s41467-024-53150-3.

Correspondence and requests for materials should be addressed to Alexander A. High.

Peer review information *Nature Communications* thanks the anonymous reviewers for their contribution to the peer review of this work. A peer review file is available.

Reprints and permissions information is available at http://www.nature.com/reprints

Publisher's note Springer Nature remains neutral with regard to jurisdictional claims in published maps and institutional affiliations.